Solar Energy Materials & Solar Cells 145 (2016) 93–103

Contents lists available at ScienceDirect

Solar Energy Materials & Solar Cells

journal homepage: www.elsevier.com/locate/solmat

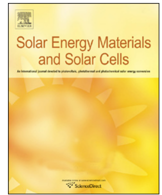

# Piezoresistivity of thin film semiconductors with application to thin film silicon solar cells

D. Lange [a,b,*], P.Roca i Cabarrocas [b], N. Triantafyllidis [a], D. Daineka [b]

[a] *Laboratoire de Mécanique des Solides, Ecole Polytechnique, Palaiseau, 91128, France*
[b] *Laboratoire de Physique des Interfaces et des Couches Minces, Ecole Polytechnique, Palaiseau, 91128, France*

ARTICLE INFO

*Article history:*
Received 8 June 2015
Received in revised form
6 August 2015
Accepted 11 September 2015
Available online 4 October 2015

*Keywords:*
Amorphous silicon
Microcrystalline silicon
Zinc oxide
ITO
Piezoresistivity
Flexible PV

ABSTRACT

The influence of mechanical strain on the conductivity (piezoresistivity) of intrinsic and doped hydrogenated amorphous and microcrystalline silicon (a-Si:H and μ-Si:H) thin films as well as indium tin oxide and aluminum doped zinc oxide is examined under uniaxial tension and compression. The aim of this work is to characterize and model the influence of stress on thin film solar cells. The resistivity of intrinsic a-Si:H and μ-Si:H as well as that of n-type a-Si:H and μ-Si:H decreases with increasing tensile strain whereas it is increasing for both p-type materials. Both ITO and ZnO:Al show no significant change in resistivity with tensile strain until a critical strain value of roughly 0.5% that initiates fracture and introduces a non-reversible resistivity increase. Such irreversible changes occur for silicon layers at higher strains (1%). Silicon nitride buffer layers decrease the value of this critical strain. Tensile tests inside a scanning electron microscope demonstrate that such irreversible changes are related to crack formation when a certain tensile strain is exceeded. Analytical and numerical calculations are performed to estimate the influence of strain on the efficiency of p-i-n solar cells, which is roughly $+/-0.3\%$ for a biaxial strain of $+/-1\%$.

© 2015 Elsevier B.V. All rights reserved.

## 1. Introduction

Strain has a strong influence on the electrical properties of silicon, namely its conductivity. This effect was first studied experimentally by Smith [1]. His work was proceeded by Bardeen and Shockley who built the theoretical foundation with their deformation potential theory [2]. Herring and Vogt applied this theory specifically to piezoresistivity to explain the experimental results of Smith [3,4]. Strain changes the electronic transport properties of silicon and other semiconductors by changing the crystal's geometry (changing bond angles and distances) and thus the band structure. This effect strongly depends on the crystal orientation with respect to the applied stress and the type of stress that is applied [5]. Strains can be introduced into photovoltaic devices during the fabrication process, the installation process and during operation for both wafer based and thin film silicon solar cells. Processes involving cooling and heating of materials with different thermal expansion coefficients like soldering [6], encapsulation and the crystal growth itself [7] lead to straining in silicon wafers. Plasma processes used for thin film depositions equally lead to non-negligible residual strains caused by differences in thermal expansion coefficients and ion bombardment. Several experimental works have shown that certain plasma conditions can lead to compressive stresses up to 1000 MPa (corresponding to a strain of roughly 0.7%) [8,9]. From the 1990s on, the strain effect on silicon has been beneficially used in transistors in form of strained silicon technology where epitaxially grown SiGe layers and silicon nitride capping layers are used to introduce strain into the channel of silicon transistors. A mobility gain of up to 30% can be realized with a strain of just 0.2% in the case of monocrystalline silicon [10]. Those methods are known as elastic strain engineering [11].

Both theoretical and experimental works have examined the effect of strain in amorphous and polycrystalline silicon layers, junctions and cells [12–16]. With the growing interest in flexible electronics, there have been as well many works on the fracture properties of both indium tin oxide (ITO) and aluminum doped zinc oxide (ZnO:Al) which are used as transparent and conducting layers. The fracture properties of these brittle materials strongly depend on the thickness of the layer and the interface quality (defect density for example). ITO of 100 nm begins to fracture at strains around 1.5% [17]. ZnO:Al fractures at the same strain for thin layers of 100 nm but already fails mechanically at a strain of 0.5% if the thickness is increased to 800 nm [18–20]. It is further known for its piezoelectric properties [21]. The influence of strain on transport properties of ITO is exploited in the fabrication of strain gauges [22].

* Corresponding author.

http://dx.doi.org/10.1016/j.solmat.2015.09.014
0927-0248/© 2015 Elsevier B.V. All rights reserved.

This work is motivated by the desire to evaluate if strain could also be used in photovoltaic cells to enhance their efficiency. This will be examined by studying the piezoresistivity of the different building blocks of a typical p-i-n cell. The influence of stress on every single layer in a typical p-i-n thin film solar cell consisting of a transparent conductive oxide, a p-type, an intrinsic, a n-type layer (either microcrystalline or amorphous) and a metal back contact was determined to achieve this goal.

We continue by giving some basic relations in the next section that are needed to model piezoresistivity. We will see that both the mobility and the intrinsic carrier concentration depend on strain. The strain dependence of the former can be deduced from our piezoresistivity measurements. We will then describe the experimental setup and the obtained results in the following two sections. The last section, before concluding this work, will be devoted to the estimation of the influence of strain the $J(V)$ characteristics of p-i-n solar cell.

## 2. Theory: piezoresistivity of thin films

The conductivity $\sigma$ of single layer semiconductors relates the electric field $E$ to the current density $J$. This is known as Ohm's law:

$$J = \sigma E \tag{1}$$

The conductivity of the semiconductor itself is a product of the charge carrier concentration and mobility:

$$\sigma = q\left(\mu_n n + \mu_p p\right) \tag{2}$$

where $\mu_n$ and $\mu_p$ are the electron and hole mobility, n and p the electron and hole concentration and q the elementary charge. The conductivity is in principle a tensor but the isotropy of an amorphous or a randomly oriented polycrystalline semiconductor reduces it to a scalar. The inverse of the conductivity is the resistivity: $\sigma = 1/\rho$. For a doped semiconductor, the charge carriers are mainly determined by the number of ionized dopants. Eq. (2) thus simplifies to:

$$\frac{1}{\rho} = q\mu_n n\ ;\ 1/\rho = q\mu_p p \tag{3}$$

The number of charge carriers available for conduction can be significantly different from the actual number of donor and acceptor atoms especially in a-Si:H because of the complicated defect structure of this material. If the crystal lattice of a semiconductor is distorted by externally applied stresses or internal residual stresses, the band structure will be altered and the resistivity will change. The effects of strain on the valence and conduction bands have been widely examined [23,24] and the main reasons for a change of mobility with strain are band gap shifts, band warping and a changed intervalley scattering rate due to the shifted bands. Due to these band structure changes, the resistivity is no longer isotropic when the material is stressed. This is why a 3D formulation of the above expressions is required. The resistivity is then described by a tensor $\rho_{ij}$ and can be expressed as the sum of the initial resistivity $\rho_0$ at zero strain plus the perturbed part $\Delta\rho_{ij}$.

$$\rho_{ij} = \rho_0 \delta_{ij} + \Delta\rho_{ij} \tag{4}$$

where $\delta_{ij}$ is the Kronecker delta. Equally Ohm's law transforms to:

$$E_i = \rho_{ij} J_j \tag{5}$$

where the electric field $E_i$ and the the current density $J_j$ are now vectors. Assuming linear dependence between $\Delta\rho_{ij}$ and the strain tensor $\epsilon_{kl}$, the piezoresistive response can be described by the elastoresistive tensor $M_{ijkl}$:

$$\Delta\rho_{ij} = \rho_0 M_{ijkl} \epsilon_{kl} \tag{6}$$

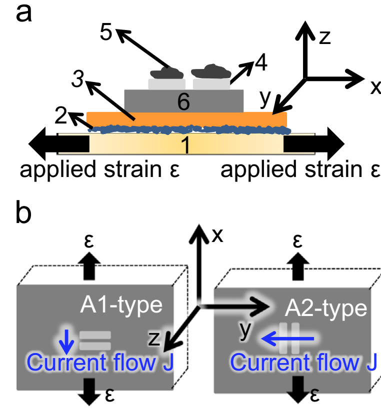


**Fig. 1.** (a) Cross section of the layer stack (dimensions are not true to scale): 1: 5 mm thick PVC substrate, 2: Alkyl cyanoacrylate adhesive, 3: 50 μm polyimide foil, 4: 150 nm aluminum contact, 5: Conductive epoxy adhesive to attach wires 6: Semiconducting layer or TCO. (b) Schematic top view of the sample. The rectangular contacts (10 mm × 5 mm, 1 mm distance) are placed in such a way that the current density $J$ is flowing either parallel (left drawing, called A1-configuration) or perpendicular (right drawing, called A2-configuration) to the applied strain ε.

For isotropic materials like amorphous materials and randomly oriented polycrystals, $M_{ijkl}$ does only have two independent constants $M_\alpha$ and $M_\beta$:

$$M_{ijkl} = M_\alpha \delta_{ij}\delta_{kl} + M_\beta(\delta_{il}\delta_{jk} + \delta_{ik}\delta_{jl}) \tag{7}$$

To determine the two constants $M_\alpha$ and $M_\beta$, we need two experiments that lead to two different stress states. The first one is identified as A1, (see also Fig. 1b) where the applied strain $\varepsilon_{xx}$ and the measured resistivity component $\Delta\rho_{xx}$ are parallel to each other. The other experiment, identified as A2, corresponds to a situation where we still apply a strain $\varepsilon_{xx}$ but where the current flows in the perpendicular direction along y and we thus determine the resistivity $\Delta\rho_{yy}$ along this direction. Eq. (7) combined with 6 thus reads for the A1-experiment as:

$$\Delta\rho_{xx} = \rho_0\left[M_\alpha(\epsilon_{xx} + \epsilon_{yy} + \epsilon_{zz}) + 2M_\beta \epsilon_{xx}\right] \tag{8}$$

Accordingly for the A2-experiment as:

$$\Delta\rho_{yy} = \rho_0\left[M_\alpha(\varepsilon_{xx} + \varepsilon_{yy} + \varepsilon_{zz}) + 2M_\beta \varepsilon_{yy}\right] \tag{9}$$

We measure both in-plane strain components $\varepsilon_{xx}$and $\varepsilon_{yy}$ (see Sections 3 and 4). Our experiments were designed to have a transverse strain component $\varepsilon_{yy}$ that is almost 0. The out-of-plane component $\varepsilon_{zz}$ is found for thin films from the requirement $T_{zz} = 0$, where $T_{ij}$ is the stress tensor. The strain component can then be expressed as $\varepsilon_{zz} = \left[\frac{-\nu}{(1-\nu)}\right](\varepsilon_{xx} + \varepsilon_{yy})$ where $\nu$ is the Poisson ratio, amounting to 0.22 for polycrystalline silicon[25]. In this case, Eqs. (8) and (9) simplify to:

$$\text{A1}-\text{experiment:}\frac{\Delta\rho_{xx}}{\rho_0} = G_L\,\varepsilon_{xx},\quad G_L \equiv M_\alpha\left(\frac{1-2\nu}{1-\nu}\right) + 2M_\beta \tag{10}$$

$$\text{A2}-\text{experiment:}\frac{\Delta\rho_{yy}}{\rho_0} = G_T\,\varepsilon_{xx},\quad G_T \equiv M_\alpha\left(\frac{1-2\nu}{1-\nu}\right) \tag{11}$$

These equations actually are expressed in terms of a quantitiy that is often used to quantify the piezoresistive properties of materials: the gauge factor $G$. Consequently we will need to measure the longitudinal gauge factor $G_L$, defined as the change of the resistance parallel to the applied strain, and the transverse gauge factor $G_T$ which quantifies the change in resistance perpendicular to the applied strain in order to obtain $M_\alpha$ and $M_\beta$. The

**Table 1**
Plasma parameters for the PECVD deposition of hydrogenated amorphous and microcrystalline silicon layers. I: intrinsic, n: n-type, p: p-type. *In order to form p-a-SiC:H, 50 sccm $CH_4$ was as well used as a precursor. **$PH_3$ and TMB are diluted at 1% in $H_2$.

| Material | RF-Power [mW/cm$^2$] | Pressure [Torr] | $H_2$ [sccm] | $SiH_4$ [sccm] | Ar [sccm] | TMB** [sccm] | PH3** [sccm] | Thickness [nm] |
|---|---|---|---|---|---|---|---|---|
| i-a-Si:H | 7.4 | 0.1 | 0 | 50 | 0 | 0 | 0 | 400 |
| n-a-Si:H | 12.3 | 0.1 | 0 | 50 | 0 | 0 | 10 | 125 |
| p-a-SiC:H* | 2 | 0.3 | 0 | 10 | 0 | 4 | 0 | 225 |
| i-μ-Si:H | 74 | 1.6 | 400 | 6 | 100 | 0 | 0 | 400 |
| n-μ-Si:H | 74 | 1.6 | 400 | 6 | 100 | 0 | 1.5 | 400 |
| p-μ-Si:H | 74 | 1.6 | 400 | 6 | 100 | 1 | 0 | 400 |

strain used to calculate the gauge factor is always the longitudinal, applied strain $\varepsilon_{xx}$.

To link the piezoresistive effect to carrier transport properties in semiconductors, we need to go back to Eq. (2), which shows that the two quantities that can possibly cause a resistivity change with strain are carrier concentration and mobility. Silicon possesses several valence and conduction bands with different effective masses and thus different mobilities. Shifting of certain energy bands with respect to others leads to a "repopulation" of electrons to energy bands with a higher mobility to those with lower mobility or vice versa. At the same time, band edge shifts will also change the intrinsic carrier concentration in semiconductors because it depends on the distance between the fermi level and the conduction and valence band. For doped semiconductors, we can separate these two effects because the carrier concentration $n$ or $p$ can be assumed to be constant due to the present dopants (see Eq. 3). In this case, there is a simple approximative relation between changing resistivity and mobility:

$$\Delta\mu_{ij}(\varepsilon)/\mu_0 \cong -\Delta\rho_{ij}(\varepsilon)/\rho_0 \tag{12}$$

We thus measure effectively the changing mobility when we measure the changing resistivity. To interpret the results of the piezoresistivity measurements of intrinsic semiconductors, we also need to know how the intrinsic carrier concentration changes with strain. The intrinsic carrier concentration can be expressed as follows [29]:

$$n_i(\varepsilon) = \sqrt{N_C N_V}\exp(-\frac{E_g(\varepsilon)}{2kT}) \tag{13}$$

where $N_C$ and $N_V$ are the number density of states in the conduction and valence band edges. We assume those quantities to be strain independent and thus constants. Strain will however shift conduction and valence bands up or down which will in turn change the band gap:

$$E_g(\varepsilon) = E_g^0 + \Delta E_g \tag{14}$$

The band edge shift $\Delta E$ of the different valence and conduction band edges can be described by deformation potentials $\Xi_{ij}$ and leads to an overall shift of the band gap $\Delta E_g$. This theory was first proposed by Bardeen and Shockley [2] and later refined by Vogt and Herring [4]. The shift of the mean energy gap for uniaxial tension can then be approximately expressed as follows [30,31]:

$$\Delta E_g = \Xi_m(\varepsilon_{xx} + \varepsilon_{yy} + \varepsilon_{zz}) \tag{15}$$

where $\Xi_m = \Xi_d + \frac{1}{3}\Xi_u - a$ is a "mean" deformation potential consisting of $\Xi_d$, the hydrostatic or "dilation" deformation potential of the conduction band, $\Xi_u$ the shear or "uniaxial" deformation potential of the conduction band and $a$ the valence band volume deformation potential at the Γ-point [32]. The dilation strain $\varepsilon_{xx} + \varepsilon_{yy} + \varepsilon_{zz}$ is given for our experiment (see Section 3, $\varepsilon_{yy} = 0$, $\sigma_{zz} = 0$ ) by $\varepsilon_{xx}\left[\frac{(1-2\nu)}{1-\nu}\right]$.

Eq. (15) is strictly speaking just valid for single crystals. We will use it however as an approximation for microcrystalline silicon in calculations we perform later. Throughout this work, a value of $\Xi_m = 1.72\text{eV}$ will be used as taken from Van de Walle et. al. [31].

The strain dependent mobility $\mu(\varepsilon)$ and the strain dependent intrinsic carrier concentration $n_i(\varepsilon)$ will later be used to estimate the strain dependent current $J(V, \varepsilon)$ through an illuminated p-i-n junction. Details of this calculation will be explained in a section that follows. The experiments explained in the next two sections serve to determine $\mu(\varepsilon)$.

## 3. Materials and methods

### 3.1. Materials

The change in resistivity of n-type, p-type and intrinsic hydrogenated amorphous (a-Si:H) and microcrystalline silicon (μ-Si:H) as well as aluminum doped zinc oxide (ZnO:Al) and indium tin oxide (ITO) with an applied tensile or compressive strain is determined. In order to perform mechanical tests, a flexible substrate was needed and we thus chose a polyimide foil (PI) substrate (50 μm DuPont™ Kapton® films) because its yield point lies at a strain of 3%. This is largely enough for our experiments because thin silicon films usually do not withstand more than 1% strain [33,25]. The PI foil was cleaned with deionized water, acetone and ethanol in an ultrasonic bath prior to depositions. All depositions of amorphous and microcrystalline layers were performed in a capacitively coupled radio-frequency (RF) plasma-enhanced chemical vapor deposition (RF-PECVD) reactor at 150 °C (Nextral D200). The deposition parameters for all silicon layers can be seen in Table 1. For some samples a protective silicon nitride (SiNx) barrier layer was deposited in the same reactor before the silicon deposition to prevent chemical interactions between the polyimide foil and the silicon layers. Silicon nitride was deposited with $N_2$, $NH_3$ and $SiH_4$ flows of 300 sccm, 54 sccm and 12 sccm at a pressure of 0.5 torr and a RF-Power of 200 W.

ZnO:Al layers (600 nm) were deposited via sputtering (Alliance Concept DP650) with an argon flow of 30 sccm at a power of 250 W whereas ITO layers (225 nm) were sputtered at an argon/oxygen flow of 43/3 sccm and at a RF-power of 200 W. Rectangular aluminum contacts (150 nm) with a width of 1 cm and a distance of 1 mm were deposited via thermal evaporation.

### 3.2. Sample preparation and mechanical tests

The polyimide foil and the deposited layers were glued onto a rigid polyvinyl chloride (PVC) substrate in order to perform mechanical tests. The process conditions lead to built-in stress (different coefficients of thermal expansion, ion bombardment, layer growth). This causes the polyimide foil with the layer on top of it to be curved after the deposition. It proved to be difficult to perform mechanical tests in this curved form. Therefore the foils were glued to a rigid substrate to make their handling easier. The adhesive used is an alkyl cyanoacrylate adhesive (M-Bond 200) that is normally used for strain gauges. It is elastic in the strain

range of plus minus 5% which is largely sufficient for our experiments. Several steps of surface preparation for the back surface of the polyimide foil and the front of the PVC substrate are necessary to guarantee a good adhesion. A roughening with sand paper is followed by cleaning with ethanol, an acidic solution and a basic solution. Wires are glued to the 2 rectangular aluminum contacts (10 mm × 5 mm) with a conductive epoxy adhesive. The cross section of the whole configuration is shown Fig. 1a.

The rectangular contacts (10 mm × 5 mm, 1 mm distance) are placed in such a way that the current is flowing either parallel (called A1-configuration) or perpendicular (called A2-configuration) to the applied strain as shown in Fig. 1b). These are the two mentioned types of experiments necessary to determine the transverse and longitudinal gauge factors $G_L$ and $G_T$ and the piezoresistive constants.

The whole layer stack was then attached to two high pressure clamps (to prevent any slippage) that are connected to a hydraulic press. The effective area to be deformed is 67 mm (width) × 10 mm (height). This is a compromise between experimental constraints (67 mm is the width of the clamps and a height less than 10 mm makes it difficult to contact the samples) and the wish to have a uniform uniaxial strain in $X$ direction with just one nonzero component of the in-plane strain ($\varepsilon_{xx}$). The design of the sample suppresses the contraction in $y$-direction that would normally happen due to a pull in $x$-direction (Poisson effect). Linear elastic calculations with the finite element software Abaqus FEA were performed in 3D in order to design a sample geometry of the PVC plate that fulfills the above mentioned requirements. A ratio $\frac{\varepsilon_{yy}}{\varepsilon_{xx}} \approx 0.01$ in the test area of our sample was calculated, which means $\varepsilon_{yy}$ is satisfyingly close to 0. Digital image correlation strain measurements later confirmed this ratio. Abaqus calculations were based on the assumption that the polyimide foil and the thin film layer stack follow the movement of the PVC substrate because the latter is much thicker than the former (5 mm versus 0.126 mm).

The specimens were then deformed to a certain displacement and a voltage was applied between the two contacts while the current was recorded. The strain of the sample was measured via digital image correlation. To use this technique, a black and white spray paint is applied between the contacts of the specimen to obtain a speckle pattern (see Fig. 2). A camera is then used to record images during the experiment. The software Vic-2D® of Correlated Solutions™ calculates the in-plane 2D stress tensor ($\varepsilon_{xx}$, $\varepsilon_{yy}$ and $\varepsilon_{xy}$) based on the positional change of the speckles.

The same kind of experiment was repeated in-situ in a scanning electron microscope chamber to link the formation of cracks or other signs of mechanical failure to a change in resistivity. The basic setup was exactly the same as for the atmospheric tests. A special stage and a smaller press allowed for in-situ testing. The substrate size changed to 24 mm (width)x35 mm (height) due to different clamps. Digital image correlation was performed on the natural contrast of the sample under SEM imaging.

In cyclic testing, two kinds of loading paths were applied. In the first one, the samples were subjected to a certain strain for 50 cycles before the strain was slightly increased and deformed again for 50 cycles. These experiments were done in the tensile regime. A second loading path subjected the samples to compressive and tensile strains that were increased by 0.1% after every cycle.

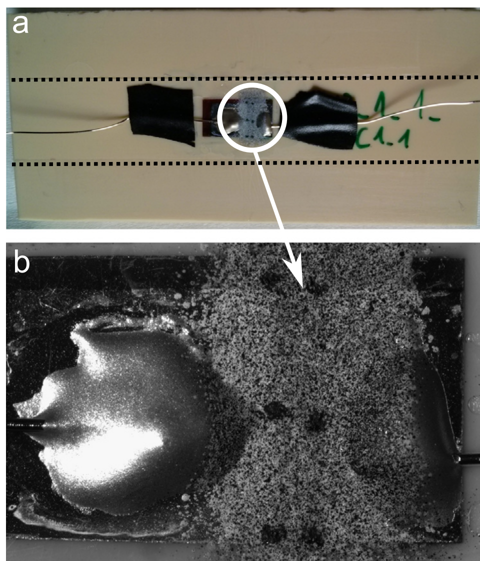


**Fig. 2.** Final sample layout with speckle pattern. (a) The dotted lines mark the area in the upper and lower part where the sample is clamped. A zoom on the center is showing (b), the speckle pattern as it is recorded for digital image correlation.

## 4. Experimental results

### 4.1. Uniaxial tests

Fig. 3 depicts the relative change of resistivity versus the applied strain in $x$-direction for the A1-experiments. Longitudinal gauge factors are indicated. The gauge factor depends on the material microstructure (amorphous, microcrystalline) and doping. First of all we can see a distinct difference between p- and n-type silicon films. It can be attributed to the different effect that strain has on conduction and valence bands and the different symmetry points of the lowest conduction and highest valence band edges. For the conduction band structure in silicon, the many valley model [3] is an accepted means to explain the piezoresistivity of these materials. Those conduction band valleys are 6 ellipsoids along the $\Delta$-symmetry-lines. They possess one heavier

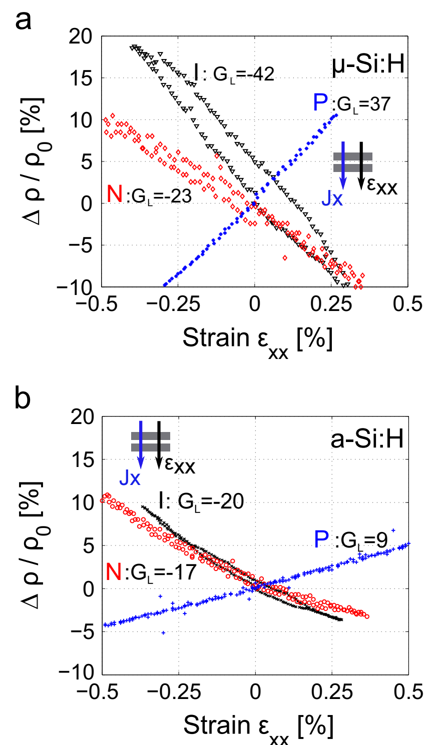


**Fig. 3.** Relative change in resistivity $\Delta\rho/\rho_0$ plotted against strain $\varepsilon_{xx}$ for the A1-configuration where applied electric field and applied strain are parallel. I stands for intrinsic, N for n-type and P for p-type silicon (a) Changes for hydrogenated microcrystalline layers. (b) Changes for hydrogenated amorphous layers.

**Table 2**
Literature data of transverse and parallel gauge factors for different amorphous and microcrystalline silicon thin films.The abbreviation n.s. stands for "not specified".

| Source | Material type | Fabrication | Gl | Gt | Maximal strain |
|---|---|---|---|---|---|
| [41] | n-type μ-Si:H | RF-PECVD | −25 | −6 | 0.04% |
| [41] | p-type μ-Si:H | RF-PECVD | 25 | 7 | 0.04% |
| [42] | p-type μ-Si:H | CMOS-MEMS | 35 | −10 | 0.01% |
| [43] | n-type μ-Si:H | HW-CVD | −14 | n.s. | 1% |
| [44] | n-type μ-Si:H | RF-PECVD | −39 | −7.6 | 0.01% |
| [44] | p-type μ-Si:H | RF-PECVD | 20.8 | −7.8 | 0.01% |
| [39] | n-type a-Si:H | Glow discharge | −18 | −7 | 0.06% |
| [39] | intrinsic a-Si:H | Glow discharge | −8 | n.s. | 0.06% |
| [39] | p-type a-Si:H | Glow discharge | 21 | n.s. | 0.06% |
| [43] | n-type a-Si:H | RF-PECVD | −18 | n.s. | 1% |

longitudinal effective mass and 2 lighter transverse effective masses. When we strain a sample, certain valleys shift up or down in energy and electrons repopulate to valleys with a lighter or higher effective mass. This leads consequently to a decreased or increased resistivity. An additional effect of strain on conduction bands is the suppression of intervalley scattering due to the band splitting [23].

The situation in the valence band at the Γ-point is a bit more complicated because it is a combined effect of band warping and splitting. In the unstrained state, there are a degenerate heavy-hole and light-hole band. This degeneracy is lifted with applied strain and additionally both bands change their shape. The biggest gauge factor in monocrystalline silicon is along <110>. Band structure calculations with the $k \cdot p$ method [34] have shown that there is a strong decrease of effective conductivity mass with compressive stress which is in good agreement with the observation that the longitudinal gauge factor is positive. The effective mass is however just a part of the picture and to have a more complete explanation of piezoresistivity in p-type silicon, scattering mechanisms must be taken into account [35].

Even though amorphous silicon has no long range order, it seems to retain the main piezoresistive properties of microcrystalline silicon. This is a hint that the local bonding configuration is still tetrahedral as in crystalline silicon. An applied uniaxial strain will change the bond angles and distances and therefore lead to a local symmetry change. The gauge factors for monocrystalline silicon actually support the general trend observed. Based on the values measured by Smith [1], the biggest gauge factor is −132 for n-type silicon along <100> and 122 for p-type silicon along <110>. The same sign for the gauge factors can be observed for the doped microcrystalline and amorphous layers just with weakened magnitudes. This is reasonable if we consider how the properties of a monorystal average in a polycrystal [36]. Assuming a randomly textured material with roughly homogeneous grain size, every orientation in the microstructure has the same weight and the grains with a preferable orientation to the applied strain dominate the piezoresistive behavior. The effect will further weaken for an amorphous material that has even less order. Consequently, the gauge factor of intrinsic amorphous silicon has the same sign as intrinsic microcrystalline silicon but the effect is weaker ($G_L = -42$, compared to $G_L = -17$, see Fig. 3a compared to 3b).

Our gauge factors for doped microcrystalline layers agree reasonably well with the values that can be found in literature which are mostly gauge factors with an absolute value around 30 as shown in Table 2. The magnitude of the gauge factor in general is however a quantity that depends on many factors such as temperature, microstructure and doping. There have been some theoretical works trying to model these dependencies [37,5,38] that agree reasonably well with experimental values and in general, the gauge factor decreases non-linearly with increasing temperature

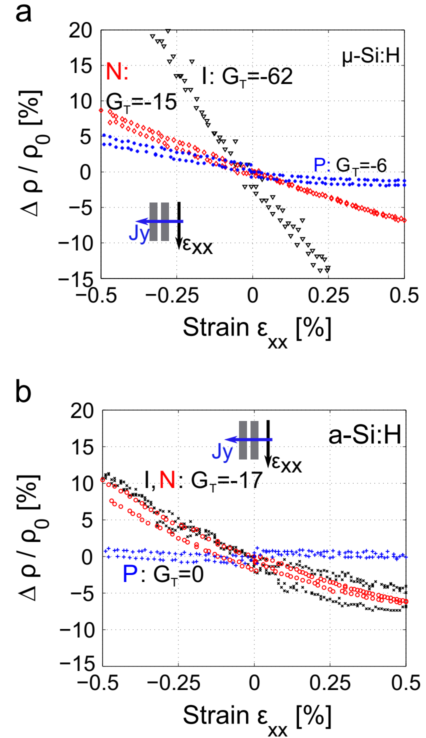


**Fig. 4.** Relative change in resistivity $\Delta\rho/\rho_0$ plotted against strain $\varepsilon_{xx}$ for the A2-configuration where applied electric field and applied strain are perpendicular to each other. I stands for intrinsic, N for n-type and P for p-type silicon (a) Changes for hydrogenated microcrystalline layers. (b) Changes for hydrogenated amorphous layers.

and doping. To the best of our knowledge, there has been no work so far on intrinsic microcrystalline silicon. In our experiments it shows even a bigger sensitivity to strain ($G = -42$ compared to $G = 37$ and $-23$) than its p- and n-type counterparts (see Fig. 3a).

There are as well not so many works on the piezoresistivity of amorphous silicon in general. Spear and Heintze [39] did the most extensive work so far and reported gauge factors for intrinsic a-Si:H that agree with ours in terms of the sign of the gauge factor and in the case of n-type a-Si:H even in the magnitude.

Both intrinsic silicon materials do behave “n-like”, meaning similar to the n-doped layers. As Eq. (2) indicates (see the theory section), conductivity for an intrinsic semiconductor is governed by the sum of the charge carrier $x$ mobility products of electrons and holes. Electrons having in general a higher drift mobility than holes [40] might be one explanation for the n-like behavior. The decrease of hole mobility with tensile strain (see the gauge factor for p-type silicon) should have an attenuating effect on the overall gauge factor of an intrinsic material. Both the gauge factor for intrinsic amorphous and microcrystalline silicon are however bigger than the n-type gauge factors. The second quantity that could change in intrinsic materials is the carrier concentration of electrons and holes (see Eq. (3)). As we will later see in more detail in Section 4.4, uniaxial tensile strain will increase the band gap and actually decrease the number of charge carriers. This should thus decrease the gauge factor on intrinsic materials compared to doped materials. We observe however that it increases. The lower impurity concentration in intrinsic materials is probably as well very important because doping usually decreases the gauge factor (increased impurity scattering) as already pointed out before.

The results of the A2 experiments are shown in Fig. 4. We observe $G_t = -15$ for n-type microcrystalline silicon and $G_t = -6$ for p-type. This enables us to calculate the piezoresistive constants $M_\alpha$ and $M_\beta$ with Eqs. (10) and (11). $M_\alpha$ amounts to -186, -45 and

-18 for intrinsic, n-type and p-type μ-Si:H whereas it amounts to -51, -51 and 0 for intrinsic, n-type and p-type a-Si:H. $M_\beta$ takes a value of 10, -4 and 21.5 for intrinsic, n-type and p-type μ-Si:H whereas it takes a value of $-1.5$, 0 and 4.5 for intrinsic, n-type and p-type a-Si:H.

The transverse gauge factor is attenuated for n-type and p-type multicrystalline layers. P-type layers additionally change the sign (compared to the longitudinal samples, Fig. 3) of the gauge factor when applied voltage and applied stress are perpendicular to each other. This effect on p-type piezoresistors is expected from other experimental (see Table 2) and theoretical works [45] even though there are a few studies that report the opposite [41,46]. Generally speaking, the piezoresistive effect weakens whenever we measure a component of the conductivity tensor (like here in our coordinate system $\sigma_{yy}$) that is not aligned with the principal value of the strain tensor (here $\varepsilon_{xx}$). This is proven by several works that successfully modeled polycrystalline conductivity by basically averaging the piezoresistive tensor [38,15].

This picture fails to explain the big transverse gauge factor of intrinsic microcrystalline silicon shown in Fig. 4a. According to what we mentioned before, intrinsic material should be influenced by both valence and conduction band changes but be governed mainly by n-like behavior. This is why it is surprising that the gauge factor does not decrease in the transverse configuration compared to the longitudinal configuration as it has been the case for n-type microcrystalline silicon (see Fig. 3 compared to Fig. 4). A big role plays very likely the changing carrier concentration due to the changing band gap (see again for more details Section 4.4) which is only an important effect in intrinsic materials. This quantity does depend on the direction of strain but not on the direction of the current [47] and is thus the same in the A2- and A1-experiments. Similarly surprising are the transverse gauge factors for n-type and intrinsic amorphous silicon which do not decrease from the parallel to the transverse configuration in contrast to the p-type material which shows no piezoresistive behavior in the transverse configuration. Observations made by other groups are contradictory. Spear and Heintze [39] reported a smaller transverse gauge factor for n-type amorphous silicon whereas Fuhs [48] measured no difference for the transverse and longitudinal intrinsic amorphous silicon.

Fig. 5 shows the effect of strain on the resistivity of transparent conductive oxides. One can see that they behave distinctively different from the silicon layers (Fig. 5 compared to Figs. 3 and 4). At the beginning of the tensile deformation the resistivity is almost not affected. The linear part of the curve we see in silicon layers is missing. Then at a critical strain, the resistivity increases sharply and upon unloading, does not return to its initial value. Both curves show a hysteresis. This behavior has most likely nothing to do with a changing band structure but more with cracks that appear perpendicular to the applied strain as observed for both ITO [17,49] and ZnO [18,21,50]. Piezoelectricity of ZnO:Al should not be an important effect because it needs an inhomogeneous strain field which is not the case for our experiments [21]. Other groups [22,51] have seen “strain gauge behavior” for ITO, meaning the linear increase or decrease of resistivity with strain. These groups mention though that the layers need to have resistivities that are higher (roughly 0.1 Ω cm) than those used in PV or flexible electronics (in our case: $10^{-4}$ Ω cm) in order to show piezoresistive behavior. These “high” resistivity samples behave still “semiconductor like” unlike our samples where the Fermi level is deep inside the conduction band and the material behaves electronically “metal like”. This is why strain does not have an influence on the electronic transport properties in our case.

The shape of our curves can be characterized by a first part where the material is unaffected up to a tensile strain of 0.5%. This is followed by a second stage where cracks are opening and the

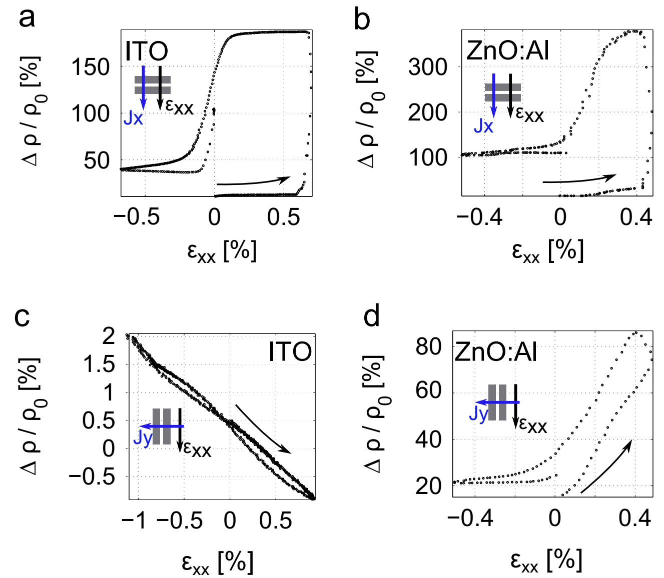


**Fig. 5.** Relative change in resistivity $\Delta\rho/\rho_0$ plotted against strain $\varepsilon_{xx}$ for the A1- and A2-configuration for ZnO:Al and ITO. The arrows mark the deformation path which is always from zero strain to tension to compression and back to zero strain. (a) Changes for ITO, A1-configuration (b) Changes for ZnO:Al, A1-configuration (c) Changes for ITO, A2-configuration (d) Changes for ZnO:Al, A2-configuration. The changes for (a)–(c) are significantly higher than for silicon due to cracking that occurs at a critical strain value.

resistivity increases because they are oriented perpendicular to the current flow which hinders the latter. After releasing the tensile strain, the cracks begin to close again but we do not see a change until the two borders of a crack physically touch and thus allow more current to flow again. The resistivity does not return to its starting value because even though the cracks are closing, they do not form a perfect atomic interface and leave defects that reduce the conductivity (reduced carrier lifetime). The results in the A2-configuration do confirm the idea that cracks are responsible for the increase in resistivity. Especially for ITO we can see that the resistivity is almost not affected if the current flows perpendicular to the strain. This can be attributed to the fact that cracks and current flow are parallel and the current can still flow in this direction. This is still true for ZnO:Al, even though the change is still considerable. This can probably be explained by cracks that start to appear parallel to the stress as also reported in literature after a certain stress level [19]. ZnO:Al is thicker (800 nm) than ITO (225 nm) in this study and this is why it probably shows a larger change of resistivity with applied strain than ITO.

### 4.2. Cycling tests

All cyclic tests were done in the A1-configuration where strain and flowing current are parallel. Fig. 6 depicts the results for a n-doped μ-Si:H sample with an intermediate silicon nitride layer. Fig. 6a) is showing 50 cycles up to a strain of 0.55% and Fig. 6b) up to 0.65%. There have been more cycles before and between these 50 cycles presented in the figure so that Fig. 6a) shows the cycles 150–200 and Fig. 6b) the cycles 250–300. There are two strain regimes observable. Up to a certain strain, the strain-resistivity behavior is repeatable and the resistivity returns to its original value after every deformation cycle ($\varepsilon = 0.55\%$). If the same sample is however subjected to a certain critical strain ($\varepsilon = 0.65\%$), a significant increase in the resistivity value (increase of $\Delta\rho/\rho_0$ by 10%) is observable and the resistivity does not fully recover. It does however stabilize after a few cycles even for the 50 cycles shown in Fig. 6b). The arguments of crack opening and closure are

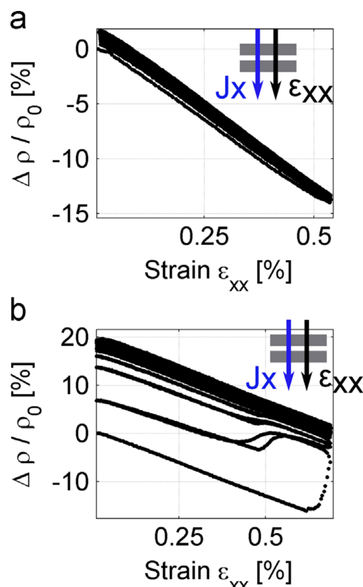


**Fig. 6.** Strain cycling of a n-doped μ-Si:H sample with an intermediate silicon nitride layer of 50 nm. Results presented in both (a) and (b) correspond to 50 cycles at the same tensile strain.

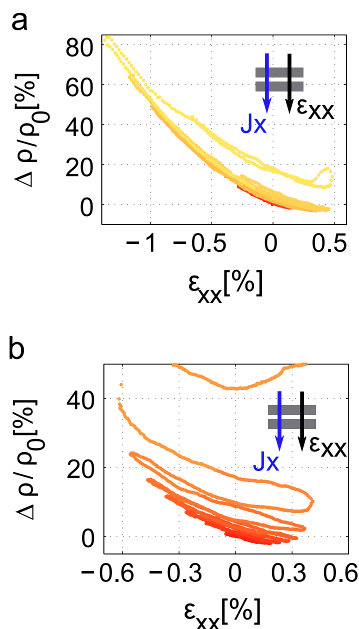


**Fig. 7.** Stepwise increasing cycling of an intrinsic amorphous silicon sample. The strain is increased by roughly 0.1% after each cycle. The color shade is changing from dark to light with every subsequent cycle (a) without silicon nitride layer (b) with silicon nitride. (For interpretation of the references to color in this figure legend, the reader is referred to the web version of this article).

basically the same as they have been for ZnO:Al and ITO. The observed behavior of silicon is a mix of the linear changes caused by band structure alterations and the non-linear and permanent increase due to cracking.

Fig. 7 compares the normalized change in resistivity of an intrinsic amorphous silicon sample directly deposited on the polyimide substrate to a sample that has an intermediate SiNx layer (50 nm) deposited as well with a RF-PECVD process in the same chamber. The strain was increased after each cycle by roughly 0.1%. What we can see is that the fracture onset strain is clearly higher for the sample without the silicon nitride layer

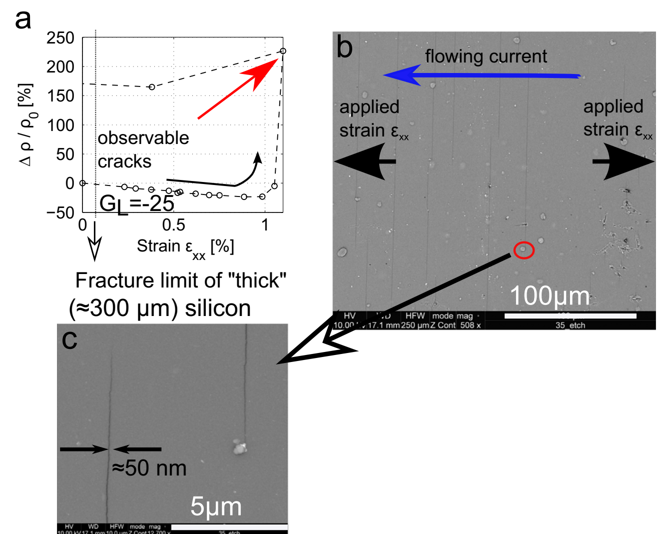


**Fig. 8.** Tensile test inside an electron microscope of a n-type μ-Si:H sample in the A1-configuration. (a) Relative change in resistivity $\Delta\rho/\rho_0$ plotted against strain $\varepsilon_{xx}$. The curved arrow marks the deformation direction. (b) Cracks started to be visible at a strain of 1.1% perpendicular to the applied strain, marked by the straight arrow (c) Zoom on an inhomogeneity that caused a crack.

(Fig. 7a). Compressive strains of more than 1% do not lead to a change in the resistivity that would indicate fracture. This is different for the sample with silicon nitride as seen in Fig. 7b). Even before reaching compressive strains of 0.6%, an irreversible change in resistivity occurs. This gets more pronounced with every cycle. The reason for this is most likely not the fracture strength of silicon nitride itself. There have been several works that actually show that the fracture strength of thin silicon nitride films is superior to the one of silicon [20,33] and can reach values of more than 2%. The reason must therefore be the interface either between amorphous silicon and silicon nitride or between silicon nitride and the polyimide surface. “Bad” interfaces can have a high concentration of defects which can drastically reduce the elastic limit of a multilayer structure because stress concentrates at these defects. We can as well observe that the film in Fig. 7b fractures first in tension. This is a usual behavior of brittle material and films that normally have a bigger fracture strength in compression compared to tension.

### 4.3. *Tensile tests in an electron microscope*

Tensile tests inside an electron microscope on a n-type μ-Si:H sample were performed to link a failure mechanism to the abrupt increase in resistivity as observed for the cycling tests. This has the advantage that we can observe the morphology of the sample surface in the micrometer range. The n-type μ-Si:H sample behaves in the same manner as the sample tested under ambient atmospheric conditions (see Fig. 8a compared to 3a) in the elastic range of the material, exhibiting a gauge factor of $G_L = -25$. A drastic rise in resistivity was observable beyond a strain $\varepsilon_{xx}$ of 0.9%. Cracks perpendicular to the applied strain started to be visible at a strain of 1.1%. The crack width, indicated by the two arrows in Fig. 8c, is in the range of 44–100 nm (the left crack in Fig. 8c is taken as an example). The question must thus be asked what caused the rise in resistivity between $\varepsilon_{xx}$=0.9–1.1% where we cannot observe cracks. Firstly, more and more cracks start to form with increasing strain. In our test, we observed just a small part of the sample. It is thus possible that cracks were already present but that they just did not originate at our observation site. It is besides possible that the initial crack size is below our observation limit.

The cracks originate favorably at inhomogeneities in the microstructure (see Fig. 8c) because stress concentrates at these points.

### 4.4. Calculation of J(V) changes with applied strain of p-i-n junctions

We will now estimate the strain dependent current density $J(V,\varepsilon)$ for a microcrystalline p-i-n junction. We will do this by using both an analytical expression taken from Taretto [52,53] and numerical calculations with the software PC1Dmod [54,55]. PC1Dmod is an open-source simulation software for solar cells that is a modified version of the original PC1D software. It solves the fully coupled non-linear equations for the quasi-one-dimensional transport of electrons and holes in semiconductor devices. It is especially suited for PV related problems. The user can define the desired geometry, physical models and material parameters.

The analytical expression from Taretto is rather complex and will thus be not shown here. It takes into account drift and diffusion currents and the voltage drop at the p-i and n-i interfaces. As most analytical expressions, it uses some assumptions to simplify the equations. Taretto assumes a “symmetrical p-i-n cell”, meaning identical mobilities $\mu$ for electrons and holes and equal majority carrier concentrations in n- and p-layers. He assumes additionally a uniform thus position-independent photogeneration rate $g$. The final expression contains further the following material parameters: surface recombination velocity $S$, layer thickness $d$, recombination lifetime $\tau$ and intrinsic carrier concentration $n_i$, The two strain dependend quantities in the $J(V,\varepsilon)$ relation are $n_i(\varepsilon)$ and $\mu(\varepsilon)$ as described in Section 2. We will stress our simulated cell biaxially in the $x$–$y$ plane. The current flows as usual in solar cells out-of plane, meaning in the $z$-direction. This is illustrated in Fig. 9 (small gray drawing). We thus calculate effectively $J_z(V,\varepsilon)$. With this configuration, $\Delta\mu_{zz}(\varepsilon)$ (Eq. 9 and Eq. 12) thus reads:

$$\Delta\mu_{zz}(\varepsilon)=\mu_0\left[M_\alpha(\varepsilon_{xx}+\varepsilon_{yy}+\varepsilon_{zz})+2M_\beta\varepsilon_{zz}\right]$$

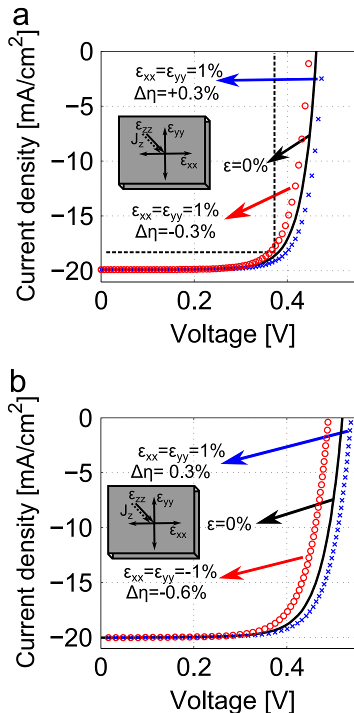


**Fig. 9.** $J(V)$-characteristic of an unstrained (solid black curve) and two strained p-i-n solar cells under illumination where crosses represent biaxial tension and circles biaxial compression. The small drawing represents the strain and current configuration. (a) Calculation obtained with the analytical model of Taretto (b) Numerical simulation with PC1Dmod.

Due to the biaxial stress, we control both $\varepsilon_{xx}$ and $\varepsilon_{yy}$. The out-of plane strain component $\varepsilon_{zz}$ can be calculated with the relation $\varepsilon_{zz}=\frac{-\nu}{1-\nu}(\varepsilon_{xx}+\varepsilon_{yy})$ which is a consequence of the plane stress present in thin films. We already pointed out in the experimental part that the gauge factor of the intrinsic layer does depend both on the change of mobility and carrier concentration and we can therefore not use the measurements for the intrinsic layer for the calculations presented here. We will thus use the piezoresistive constants $M_\alpha$ and $M_\beta$ for p- and n-layers that have been calculated from the gauge factors in Figs. 3 and 4 and were mentioned in the results section. We must however note that the isotropy assumption we used in Section 2 for microcrystalline materials could be wrong because we are dealing with thin films and they might have different properties in the out-of-plane direction. Isotropy is however not an unlikely case for microcrystalline materials with small grain size. The strain dependent carrier concentration is calculated by Eqs. ((13)–15) and with a mean deformation potential of $\Xi_m=1.72$ eV[31]

The p-i-n layer stack consists of an intrinsic layer of 1.15 μm which is sandwiched by thin doped layers of 20 nm. The material parameters for the p-i-n device used are based on a real cell by Pieters et al. [56] that Taretto used to validate his model. The doped layers are considerably thinner (10–20 nm) than the intrinsic layer so that their contribution to the overall current can be neglected. Contacts are assumed to be perfectly ohmic. The other, strain independent material parameters amount to: $S=10^4$cm/s, $\tau_n=\tau_p=70$ ns, $n=p=10^{18}$cm$^{-3}$, $\mu_n=50$ cm$^2$/Vs, $\mu_p=15$cm$^2$/Vs, $g=1.1\times10^{21}$ cm$^{-3}$. The analytical model needs a single mobility as input, which is consequentially the ambipolar mobility of 23 cm$^2$/Vs. This mobility is recalculated for the biaxially strained layers with the updated values of n- and p-type mobility. Otherwise the input parameters are the same for the analytical and numerical calculation. The strain we chose to be used for the above equations is what we consider to be a “realistic” elastic limit of the whole cell based on our experiments and on observations made by other works. We observed an elastic limit of both TCOs a little above a strain of 0.4%. Other works cited in the introduction have however shown that an elastic deformation of more than 1% is possible if the thickness is reduced and the deposition optimized. Microcrystalline silicon can show elastic behavior (see SEM experiment) up to a strain of 1%. A strain $\varepsilon_{xx}=\varepsilon_{yy}=\pm1\%$ seems thus reasonable for an upper limit and a “best-case-estimate”.

The effect of this strain configuration on the $J(V)$ characteristics of the p-i-n solar cell is shown in Fig. 9 for the analytical calculation, Fig. 9a, and numerical calculation, Fig. 9b. The current density is plotted against the applied voltage. Three strain configurations are depicted: Zero strain (solid black curve), biaxial strain of 1% (crosses) and −1% (circles). We can see that the efficiency is increasing for tensile strain (+0.3% for both methods) and decreasing for compressive strain (−0.3% for the analytical calculation and −0.6% for the numerical simulation. The general trend both for the analytical model in Fig. 9a and the numerical simulation in Fig. 9b is thus the same. The difference in predicted efficiency change for a compressive strain can be attributed to the fact that the analytical model uses a single mobility whereas the numerical model distinguishes between electron and holes.

The short circuit current does show only negligible changes (±0.02 mA/cm$^2$) for both the analytical and the numerical calculation. The charge carriers in the modeled device have already in their unstrained state a diffusion length that exceeds the device thickness. Any additional gain in mobility will not add any

additional collected charge carriers. It is thus mainly the dark current that is responsible for the efficiency change. The dark current depends linearly on the product of mobility times charge carrier concentration. Both quantities change quite considerably. If we take for example a tensile strain of $\varepsilon_{xx} = \varepsilon_{yy} = 1\%$, the intrinsic carrier concentration is decreasing by $-37\%$ (according to Eq. 13), electron mobility decreases by 20% and hole mobility increases by 10%. These changes lead to a decrease in dark current for a given voltage. Photocurrent and dark current oppose each other and a decreasing dark current is thus shifting the whole $J(V)$ curve to the right. This is why the open circuit voltage increases with tensile strain (by $+0.02$ V for both the analytical and numerical calculation). The "small" overall efficiency gain is a consequence of several possible factors. One of them is the operating point of solar cells. They are operated at the maximum power point which, for the unstrained cell (solid curve), is marked by dashed lines in Fig. 9. The changes between the strained and unstrained $J(V)$ curves become more pronounced after this point but at this point itself, the difference between the curves is marginal. Another reason for the "small" gain in efficiency is the opposite sign of the gauge factors of p- and n-type silicon. This inevitably leads to some "cancellation effect" where the gain in mobility of one carrier type cancels out the other. We will further discuss the implications of these findings in the next section.

### 4.5. Silicon PV and the possibilities of strain induced efficiency enhancement

Besides the discussed open questions regarding the gauge factors (for example the transverse gauge factors), we can see that the order of magnitude and the sign of the resistivity changes is consistent with other published studies and allows us to estimate a possible influence of strain on the characteristics of PV devices. The results obtained actually indicate that there is not a "big" change in the efficiency of PV devices at relatively high strain (=close to the elastic limit of silicon): at most around 0.3%. This is also what Jones et. al. observed for thin film amorphous triple junction cells [12]. We can further cross-check our findings against observations that Creemer et al. made for the influence of stress on the saturation current of bipolar silicon transistors [16]. The physical situation is basically the same and the basic changes they discuss are as well the mobility and charge carrier concentration. They observe changes of about 6% in the saturation current for a stress of 150 MPa. We observe similar changes in the saturation current for this stress level. This is simply not translating to big changes in solar cell efficiency. Two simple reasons for this observation were already mentioned in the previous section: The "cancellation effect" due to the opposite piezoresistive behavior of electrons and holes as well as the operating point of solar cells.

It must be noted that the situation we assumed is one for "good quality" solar cells, meaning cells with a diffusion length exceeding the device thickness. We can probably expect larger changes if this assumption is not true because strain would increase the diffusion length and thus the amount of collected carriers (bigger $J_{SC}$). This is however not a realistic situation for microcrystalline materials because for thin devices as we examine them, the diffusion length is usually much longer than the device thickness. The calculations for the p-i-n cell for example were based on a 6.9% efficient cell with a hole diffusion length of 10 μm which is already 9 times bigger than the thickness of 1.15 μm. Another factor we neglected in our calculations but which might change as well the device characteristics is the changing resistance of n- and p-type layers at both ends of the p-i-n stack. This resistance will of course as well change but was not taken in account in the models we used.

Another question that must be asked is how the strain assumed in our calculations could be implemented in a real device. This implementation would most likely be realized through residual process stress because this kind of stress is permanent unlike the externally applied stresses in our experiments. For devices deposited by plasma methods like PECVD, intrinsic stresses due to the impinging ions and the growth process itself are present depending on the deposition conditions. Based on the measurements of several groups [9,8], we can expect residual strains up to 0.7%. It is basically with such processes that the desired strain is realized in strained transistor structures, either with embedded SiGe or with silicon nitride capping layers. Another general source of stress in solar cells is the cooling of a multilayer structure with different thermal expansion coefficients. We could imagine that this is beneficially used to introduce stresses into the structure (see for example the work of Hsueh [57] for analytical solutions to such a multilayer problem). One example is the cooling of the encapsulant in solar cell devices. Eitner et al. [58] estimated this stress to be $-76$ MPa in "classical" crystalline silicon cells.This is too small in terms of strain engineering but it is imaginable that this is as well tunable depending on the thermal expansion coefficients and thicknesses of encapsulant material, substrate and deposited layers.

Our results provide an important estimate of the "flexibility" of the materials used in this study and thus their possible use in flexible electronics. The upper strain limit is set by the transparent conductive oxides at a strain of roughly 0.5%. Silicon could withstand higher strain values but a lot of care must be taken to interfaces present in the devices because they might decrease this elastic limit. The strain in bent devices or layers is related to the curvature by $\varepsilon = \frac{t}{2R}$ where $R$ is the bending radius and $t$ the device thickness. Simple calculations show that for a substrate of 50 μm and device layers in the low micrometer range as presented in this work, a curvature of roughly less than 1 $cm^{-1}$ can be applied to a layer with an elastic limit of 0.5%. We already mentioned that it is imaginable to increase this limit further by optimizing the different layers. A radius of 1 $cm^{-1}$ is however already enough for applications like roll-to-roll processing or even transportable solar cells for outdoor activities.

## 5. Conclusions

We have determined the transverse and longitudinal gauge factors for all materials present in a typical a-Si:H or μ-Si:H p-i-n solar cell. Intrinsic and n-type layers show a decreasing resistivity with increasing tensile strain whereas the p-type layer shows an opposite behavior. This is attributed to the different ways strain affects valence and conduction bands. Longitudinal gauge factors for intrinsic, n-type and p-type μ-Si:H are $-42$, $-23$ and 37 respectively, whereas they are $-20$, $-17$ and 9 for intrinsic, n-type and p-type a-Si:H. The stress-limiting layers in a p-i-n cell will most likely be the transparent conductive oxides because both ITO and ZnO:Al already show an irreversible resistivity increase (which is most likely linked to cracks) at a strain of about 0.5%. Silicon layers can withstand higher strains (up to roughly 1% in tension and compression) but this has shown to change with an intermediate silicon nitride layer which decreases the fracture onset strain (to 0.6%). In-situ SEM tensile tests with n-type μ-Si:H have proven the origin of irreversible resistivity changes to be cracks perpendicular to the applied strain.

The measured strain gauge values have been used to calculate strain induced mobility changes whereas deformation potentials have been utilized to predict the change of the intrinsic carrier concentration. Both quantities together served to estimate a possible influence of an applied external strain on the $J(V)$

characteristic of p-i-n solar cells. We used both analytical expressions and PC1Dmod calculations to estimate this change. These calculations have shown similar changes regardless of the calculation method. Absolute changes in efficiency of at most $+/-0.3\%$ are predicted for biaxial strains of $+/-1\%$.

## Acknowledgments

The authors wish to thank Ecole Polytechnique which financed this work through a Monge Scholarship for the first author. We would also like to thank the staff of both the Laboratoire de Mécanique des Solides and the Laboratoire de Physique des Interfaces et des Couches Minces at Ecole Polytechnique for various support. The Kapton® substrates were generously provided by Du Pont® for research purposes.

## Bibliography

[1] C.S. Smith, Piezoresistance effect in Germanium and Silicon, Phys. Rev. 94 (1954) 42–49.
[2] J. Bardeen, W. Shockley, Deformation potentials and mobilities in non-polar crystals, Phys. Rev. 80 (1950) 72–80.
[3] C. Herring, Transport properties of a many-valley semiconductor, Bell Syst. Tech. J. 34 (1955) 237–290, http://dx.doi.org/10.1002/j.1538-7305.1955.tb01472.x.
[4] C. Herring, E. Vogt, Transport and deformation-potential theory for many-valley semiconductors with anisotropic scattering, Phys. Rev. 101 (1956) 944–961.
[5] Y. Kanda, A graphical representation of the piezoresistance coefficients in silicon, IEEE Trans. Electron Devices (1982) 64–70.
[6] B. Jaeckel, A. Pfennig, M. Mette, M. Träger, J. Wendt, The link between mechanical stress induced by soldering and micro damages in silicon solar cells, in: Proceedings of the 24th European Photovoltaic Solar Energy Conference Hamburg, Ger., 21–25 Sept. 2009, pp. 3420–3423. 10.4229/24thEUPVSEC2009-4AV.3.40.
[7] S. He, S. Danyluk, I. Tarasov, S. Ostapenko, Residual stresses in polycrystalline silicon sheet and their relation to electron-hole lifetime, Appl. Phys. Lett. 89 (2006) 111909, http://dx.doi.org/10.1063/1.2354308.
[8] Y.Q. Fu, J.K. Luo, S.B. Milne, aJ. Flewitt, W.I. Milne, Residual stress in amorphous and nanocrystalline Si films prepared by PECVD with hydrogen dilution, Mater. Sci. Eng. B 124–125 (2005) 132–137, http://dx.doi.org/10.1016/j.mseb.2005.08.104.
[9] V. Paillard, P. Puech, R. Sirvin, S. Hamma, P. Roca, I. Cabarrocas, Measurement of the in-depth stress profile in hydrogenated microcrystalline silicon thin films using Raman spectrometry, J. Appl. Phys. 90 (2001) 3276–3279, http://dx.doi.org/10.1063/1.1396828.
[10] S.E. Thompson, M. Armstrong, C. Auth, S. Cea, R. Chau, G. Glass, et al., A logic nanotechnology featuring strained-silicon, IEEE Electron Device Lett. 25 (2004) 191–193.
[11] Elastic Strain Engineering Unprecedented Materials Properties, in: J. Li, Z. Shan, E. Ma, G. (Eds.), MRS Bulletin, http://dx.doi.org/10.1557/mrs.2014.3.
[12] R. Jones, T. Johnson, W. Jordan, S. Wagner, J. Yang, G. Subhendu, Effects of mechanical strain on the performance of amorphous silicon triple-junction solar cells, in: Proceedings of the Twenty-ninth IEEE Photovoltaic Specialists Conference Rec., 2002, pp. 1214–1217.
[13] M. Utsunomiya, A. Yoshida, Effect of mechanical strain on electrical characteristics of hydrogenated amorphous silicon junctions, J. Appl. Phys. 66 (1989) 308, http://dx.doi.org/10.1063/1.343874.
[14] H. Gleskova, P.I. Hsu, Z. Xi, J.C. Sturm, Z. Suo, S. Wagner, Field-effect mobility of amorphous silicon thin-film transistors under strain, J. Non-Cryst. Solids 338–340 (2004) 732–735, http://dx.doi.org/10.1016/j.jnoncrysol.2004.03.079.
[15] P.J. French, A.G.R. Evans, Piezoresistance in polysilicon, Electron. Lett. 20 (1984) 999–1000.
[16] J.F. Creemer, F. Fruett, G.C.M. Meijer, S. Member, P.J. French, A. Member, The piezojunction effect in silicon sensors and circuits and its relation to piezoresistance, IEEE Sens. J. 1 (2001) 98–108.
[17] M.N. Saleh, G. Lubineau, Solar energy materials & solar cells understanding the mechanisms that change the conductivity of damaged ITO-coated polymeric fi lms : a micro-mechanical investigation, Sol. Energy Mater. Sol. Cells 130 (2014) 199–207, http://dx.doi.org/10.1016/j.solmat.2014.07.011.
[18] K.A. Sierros, D.A. Banerjee, N.J. Morris, D.R. Cairns, I. Kortidis, G. Kiriakidis, Mechanical properties of ZnO thin films deposited on polyester substrates used in flexible device applications, Thin Solid Films 519 (2010) 325–330, http://dx.doi.org/10.1016/j.tsf.2010.07.081.
[19] E. Fortunato, P. Nunes, a Marques, D. Costa, H. Águas, I. Ferreira, et al., Influence of the strain on the electrical resistance of zinc oxide doped thin film deposited on polymer substrates, Adv. Eng. Mater. 4 (2002) 610–612 10.1002/1527-2648(20020806)4:8 < 610::AID-ADEM610 > 3.0.CO;2-1.
[20] K. Matoy, H. Schönherr, T. Detzel, T. Schöberl, R. Pippan, C. Motz, et al., A comparative micro-cantilever study of the mechanical behavior of silicon based passivation films, Thin Solid Films 518 (2009) 247–256, http://dx.doi.org/10.1016/j.tsf.2009.07.143.
[21] Z.L. Wang, J. Song, Piezoelectric nanogenerators based on zinc oxide nanowire arrays, Science 312 (2006) 242–246, http://dx.doi.org/10.1126/science.1124005.
[22] S.E. Dyer, O.J. Gregory, P.S. Amons, A.B. Slot, Preparation and piezoresistive properties of reactively sputtered indium tin oxide thin films, Thin Solid Films 288 (1996) 279–286, http://dx.doi.org/10.1016/S0040-6090(96)08865-7.
[23] M.L. Lee, E. a Fitzgerald, M.T. Bulsara, M.T. Currie, A. Lochtefeld, Strained Si, SiGe, and Ge channels for high-mobility metal-oxide- semiconductor field-effect transistors, J. Appl. Phys. 97 (011101) (2005) 1–27, http://dx.doi.org/10.1063/1.1819976.
[24] Y. Sun, S.E. Thompson, T. Nishida, Physics of strain effects in semiconductors and metal-oxide-semiconductor field-effect transistors, J. Appl. Phys. 101 (2007) 104503, http://dx.doi.org/10.1063/1. 2730561.
[25] W.N.J. Sharpe, B.Y. Bin, Yuan R., Vaidyanathan R.L. Edwards, Measurements of Young's modulus, Poisson's ratio, and tensile strength of polysilicon, in: Proceedings of the IEEE Tenth Annu. Int. Work. Micro Electro Mech. Syst. An Investig. Micro Struct. Sensors, Actuators, Mach. Robot., 429, 1997, pp. 424–429. doi: 10.1109/MEMSYS.1997.581881.
[29] S.M. Sze, K.K. Ng, Physics of Semiconductor Devices, John Wiley & Sons, 2006. 〈https://books.google.com/books?id=o4unkmHBHb8C&pgis=1〉 (accessed 12.4.2015).
[30] I. Balslev, Influence of uniaxial stress on the indirect absorption edge in silicon and germanium,, Phys. Rev. 143 (1966) 636–647, http://dx.doi.org/10.1103/PhysRev.143.636.
[31] C.G. Van De Walle, R.M. Martin, Theoretical calculations of heterojunction discontinuities in the Si/Ge system, Phys. Rev. B 34 (1986) 5621–5634.
[32] M. Cardona, N.E. Christensen, Acoustic deformation potentials and heterostructure band offsets in semiconductors, Phys. Rev. B 35 (1987) 6182–6194, http://dx.doi.org/10.1103/PhysRevB.35.6182.
[33] J. Gaspar, M.E. Schmidt, J. Held, O. Paul, Wafer-scale microtensile testing of thin films, J. Microelectromech. Syst. 18 (2009) 1062–1076, http://dx.doi.org/10.1109/JMEMS.2009.2029210.
[34] T. Guillaume, M. Mouis, Calculations of hole mass in [110]-uniaxially strained silicon for the stress-engineering of p-MOS transistors, Solid State Electron. 50 (2006) 701–708, http://dx.doi.org/10.1016/j.sse.2006.03.040.
[35] J. Richter, J. Pedersen, M. Brandbyge, E.V. Thomsen, O. Hansen, Piezoresistance in p-type silicon revisited, J. Appl. Phys. 104 (023715) (2008) 1–8, http://dx.doi.org/10.1063/1.2960335.
[36] P. Alpuim, M. Andrade, V. Sencadas, M. Ribeiro, S.A. Filonovich, S. Lanceros-Mendez, Piezoresistive properties of nanocrystalline silicon thin films deposited on plastic substrates by hot-wire chemical vapor deposition, Thin Solid Films 515 (2007) 7658–7661, http://dx.doi.org/10.1016/j.tsf.2006.11.138.
[37] P.J. French, A.G.R. Evans, Polycrystalline silicon as a strain gauge material, J. Phys. E 1055 (1986) 1–5, http://dx.doi.org/10.1088/0022-3735/19/12/016.
[38] M. Le Berre, M. Lemiti, M. Barbier, P. Pinard, J. Cali, E. Bustarret, et al., Piezoresistance of boron-doped PECVD and LPCVD polycrystalline silicon films, Sens. Actuators A 46–47 (1995) 166–170.
[39] W.E. Spear, M. Heintze, The effects of applied and internal strain on the electronic propertiesof amorphous silicon, Philos. Mag. Part B 54 (1986) 343–358, http://dx.doi.org/10.1080/13642818608236853.
[40] T. Dylla, F. Finger, E. a Schiff, Hole drift-mobility measurements in microcrystalline silicon, Appl. Phys. Lett. 87 (2005) 32103–32105, http://dx.doi.org/10.1063/1.1984087.
[41] P. Alpuim, J. Gaspar, P. Gieschke, C. Ehling, J. Kistner, N.J. Gonçalves, et al., Study of the piezoresistivity of doped nanocrystalline silicon thin films, J. Appl. Phys. 109 (2011) 123717, http://dx.doi.org/10.1063/1.3599881.
[42] T.-K. Kang, Evaluation of p-type polysilicon piezoresistance in a full-bridge circuit for surface stress sensors, Measurement 61 (2015) 243–248, http://dx.doi.org/10.1016/j.measurement.2014.10.054.
[43] J. Gaspar, A. Gualdino, B. Lemke, O. Paul, V. Chu, J.P. Conde, Mechanical and piezoresistive properties of thin silicon films deposited by plasma-enhanced chemical vapor deposition and hot-wire chemical vapor deposition at low substrate temperatures, J. Appl. Phys. 112 (024906) (2012) 1–8, http://dx.doi.org/10.1063/1.4736548.
[44] S. Nishida, M. Konagai, K. Takahashi, Piezoresistive effect of hydrogenated microcrystalline silicon prepared by plasma- and photo-chemical vapor deposition, Jpn. J. Appl. Phys. 25 (1986) 17–21, http://dx.doi.org/10.1143/JJAP.25.17.
[45] V. a Gridchin, V.M. Lubimsky, M.P. Sarina, Piezoresistive properties of polysilicon films, Sens. Actuators A Phys. 49 (1995) 67–72, http://dx.doi.org/10.1016/0924-4247(95)01013-Q.
[46] D. Schubert, W. Jenschke, T. Uhlig, F.M. Schmidt, Piezoresistive properties of polycrystalline and crystalline silicon films, Sens. Actuators 11 (1987) 145–155, http://dx.doi.org/10.1016/0250-6874(87)80013-6.
[47] J.F. Creemer, P.J. French, Piezojunction effect in bipolar transistors at moderate stress levels: a theoretical and experimental study, Sens. Actuators A Phys. 82 (2000) 181–185, http://dx.doi.org/10.1016/S0924-4247(99)00362-3.
[48] W. Fuhs, Influence of pressure on the electronic conduction in tetrahedrally bonded amorphous semiconductors, Phys. Status Solidi 10 (1972) 201–207, http://dx.doi.org/10.1016/0042-207X(73)90564-2.

[49] J.W. Park, G. Kim, S.H. Lee, E.H. Kim, G.H. Lee, The effect of film microstructures on cracking of transparent conductive oxide (TCO) coatings on polymer substrates, Surf. Coat. Technol. 205 (2010) 915–921, http://dx.doi.org/10.1016/j.surfcoat.2010.08.055.
[50] J.L. Ni, X.F. Zhu, Z.L. Pei, J. Gong, C. Sun, G.P. Zhang, Comparative investigation of fracture behaviour of aluminium-doped ZnO films on a flexible substrate, J. Phys. D Appl. Phys. 42 (2009) 175404, http://dx.doi.org/10.1088/0022-3727/42/17/175404.
[51] O.J. Gregory, Q. Luo, J.M. Bienkiewicz, B.M. Erwin, E.E. Crisman, An apparent n to p transition in reactively sputtered indium-tin-oxide high temperature strain gages, Thin Solid Films 405 (2002) 263–269, http://dx.doi.org/10.1016/S0040-6090(01)01703-5.
[52] K. Taretto, New explicit current/voltage equation for p-i-n solar cells including interface potential drops and drift/ diffusion transport, Prog. Photovolt. Res. Appl. 22 (2014) 870–884, http://dx.doi.org/10.1002/pip.2325.
[53] K. Taretto, U. Rau, J.H. Werner, Closed-form expression for the current/voltage characteristics of pin solar cells, Appl. Phys. A 77 (2003) 865–871.
[54] H. Haug, B.R. Olaisen, Ø. Nordseth, E.S. Marstein, A graphical user interface for multivariable analysis of silicon solar cells using scripted PC1D simulations, Energy Procedia 38 (2013) 72–79, http://dx.doi.org/10.1016/j.egypro.2013.07.251.
[55] D.A. Clugston, P.A. Basore, PC1D version 5: 32- bit solar cell modeling on personal computers, Conf. Rec., in: Proceedings of the IEEE Twenty Sixth Photovolt. Spec. Conf., 1997, pp. 207–210. 10.1109/PVSC.1997.654065.
[56] B.E. Pieters, H. Stiebig, M. Zeman, R.A.C.M.M. van Swaaij, Determination of the mobility gap of intrinsic μc-Si:H in p-i-n solar cells, J. Appl. Phys. 105 (2009) 044502, http://dx.doi.org/10.1063/1.3078044.
[57] C.H. Hsueh, Thermal stresses in elastic multilayer systems, Thin Solid Films 418 (2002) 182–188.
[58] U. Eitner, S. Kajari-Schröder, M. Köntges, H. Altenbach, Thermal stress and strain of solar cells in photovoltaic modules, in: H. Altenbach, V.A. Eremeyev (Eds.), Shell-like Structures, Springer, Berlin, Heidelberg, http://dx.doi.org/10.1007/978-3-642-21855-2.